

# Interacting scalar tensor cosmology in light of SNeIa, CMB, BAO and OHD observational data sets

Sayed Wrya Rabiei<sup>a,1</sup>, Haidar Sheikhhahmadi<sup>b,1,2</sup>, Khaled Saaidi<sup>c,1,3</sup>, Ali Aghamohammadi<sup>d,4</sup>

<sup>1</sup>Department of Physics, Faculty of Science, University of Kurdistan, Sanandaj, Iran.

<sup>2</sup>Institute for Advance Studies in Basic Sciences (IASBS) Gava Zang, Zanjan 45137-66731, Iran.

<sup>3</sup>Science and Technology Park of Kurdistan, Sanandaj, Iran.

<sup>4</sup>Sanandaj Branch Islamic Azad University, Iran.

Received: date / Accepted: date

**Abstract** During this work, an interacting chameleon like scalar field scenario, by considering SNeIa, CMB, BAO and OHD data sets is investigated. In fact, the investigation is realized by introducing an ansatz for the effective dark energy equation of state, which mimics the behaviour of chameleon like models. Based on this assumption, some cosmological parameters including Hubble, deceleration and coincidence parameters in such mechanism are analysed. It is realized that, to estimate the free parameters of a theoretical model, by regarding the systematic errors it better the whole of the above observational data sets to be considered. In fact, if one considers SNeIa, CMB and BAO but disregards OHD it maybe leads to different results. Also to get a better overlap between the counters with the constraint  $\chi_m^2 \leq 1$ , the  $\chi_T^2$  function could be re-weighted. The relative probability functions are plotted for marginalized likelihood  $\mathcal{L}(\Omega_{m0}, \omega_1, \beta)$  according to two dimensional confidence levels 68.3%, 90% and 95.4%. Meanwhile, the value of free parameters which maximize the marginalized likelihoods using above confidence levels are obtained. In addition, based on these calculations the minimum value of  $\chi^2$  based on free parameters of an ansatz for the effective dark energy equation of state are achieved.

**PACS** 98.80.-k · 98.80.Es · 95.36.+x

## 1 Introduction

Observational data sets including Cosmic Microwave Background(CMB) [1, 2], Supernovae type Ia (SNeIa) [3, 4], Baryonic Acoustic Oscillations (BAO) [5, 6], Observational Hubble Data (OHD) [7, 8], Sloan Digital Sky Survey (SDSS) [9,

10], and Wilkinson Microwave Anisotropy Probe (WMAP) [11, 12], are considered as criterion for accuracy of theoretical models. Amongst these constraints, the CMB and SNeIa( because of abundance of their data sources) attract more attention. It is notable, the SNeIa constraint in high redshift values do not give a good clue to investigate the evolution of the Universe. It is obvious the results of individual observations give different values for free parameters of a theoretical model; hence, it is better that, to estimate the best quantities for free parameters of the model one considers the whole of observational data sets including CMB, SNeIa, BAO and OHD. Therefore, this motivated us to study the behaviour of free parameters and their overlaps. Thence, a collective of observations including SNeIa, CMB, BAO and OHD are considered. Meanwhile the mentioned observational data sets have predicted an ambiguous form of matter which leads to an accelerated phase of present epoch and it is well known as dark energy. Based on this ambiguous form of matter, scientists have proposed different proposals up to now. Amongst all of those proposals, the cosmological constant,  $\Lambda$ , model attracts more attention [13, 14]. But this mechanism suffers two well known drawbacks. The first of them is related to estimate the contribution of quantum fluctuation of zero point energy and second is related to the ratio of  $\Lambda$  and dark matter energy densities. These problems and also the excellent work by Brans and Dicke [15] motivated scientists to introduce a mechanism which  $\Lambda$  had time dependency, namely quintessence [16, 17, 18]. Beside the quintessence mechanism, some proposals which risen from quantum gravity or string theory are introduced to estimate cosmological parameters. For instance one can refer to tachyon [19, 20], phantom [21, 22, 23], quintum [24, 25], k-essence [26, 27] and so on. Also some models which were risen from quantum field fluctuations or space time fluctuations attract more attention to investigate dark energy concept. For such models, one can

<sup>a</sup>e-mail: wrabiei@uok.ac.ir

<sup>b</sup>e-mail: h.sh.ahmadi@gmail.com/ h.sh.ahmadi@iasbs.ac.ir

<sup>c</sup>e-mail: ksaaidi@uok.ac.ir

<sup>d</sup>e-mail: a.aghamohammadi@iausdj.ac.ir

mention Zero Point Quantum Fluctuations(ZPQF) [28,29,30], Holographic Dark Energy(HDE) [31,32,33,34,35,36], Agegraphic Dark Energy (ADE) and new-ADE [37,38,39]. If scalar field, in the quintessence model couples to matter (non relativistic) it induces to appear a fifth force. When the coupling is of order unity, the results of strongly coupling scalar field is not in good agreement with local gravity tests (for instance in solar system). Thus a mechanism should be exist to suppress the effect of fifth force; such mechanism is capable to reconcile strong coupling models with local experiments was proposed by Khoury and Weltman [40,41] and also, separately, by Mota and Barrow [42] namely chameleon. In this mechanism, one can not choose an arbitrary Lagrangian for matter,  $L_m$ . To avoid deviation of geodesic trajectory, the author of [43] has shown the best choices are  $L_m = P$  and  $L_m = -\rho$ , where  $P$  is pressure and  $\rho$  is energy density of matter, for more discussion we refer reader to [44,45,46]. Therefore main motivation of this work is investigation the behavior of an interacting scalar field mechanism; based on these calculations and SNeIa, CMB, BAO and OHD data sets the minimum value of  $\chi^2$  for the effective dark energy equation of state are achieved. The scheme of the paper is as follows:

The above discussions which are brief review about observational and theoretical motivations are considered as introduction. In Sec. 2, the general theoretical discussions risen from a chameleon like mechanism related to the cosmological parameters such as Hubble, deceleration and coincidence parameters will be discussed. In Sec. 3, a brief review about cosmological data sets are brought. In Sec. 4, the observational data sets including SNeIa, CMB, BAO and OHD are considered, to estimate the minimum value of  $\chi^2$  related to free parameters of an ansatz for the effective dark energy equation of state. And at last, Sec.5, is dedicated to concluding remarks.

## 2 Conservation and field's equations in an effective dark energy scenario

In chameleon like scalar field scenario, the mass of scalar field is a function of local matter density, so that, it is sufficiently large on dense environment. Due to this fact, the equivalence principal (EP) is satisfied in the laboratory [40,41]. In addition, the Brans Dicke  $\omega$  parameter for two observational values of  $\gamma$  post Newtonian parameter take the values of order  $10^4$  [47], which satisfies the solar system constraint. The chameleon like scenario is defined as

$$S = \int d^4x \frac{1}{2} \sqrt{-g} (R - \partial^\mu \phi \partial_\mu \phi - 2V(\phi) + 2f(\phi)L), \quad (1)$$

[43,44,48,49,50,51,52]. In this equation  $g$  is the determinant of the metric,  $V(\phi)$  is a run away potential and the latest term indicates a non-minimal coupling between scalar field

and matter sector. It should be noted  $L$  is the Lagrangian density of matter which consists of both dark matter and dark energy sectors as perfect fluid [47,48,49,52,53]. It should be noticed that, background is a spatially flat Friedmann-Limaitre-Robertson-Walker (FLRW) Universe, with signature  $(+2)$ . The variation of the action 1, with respect to (w.r.t)  $g_{\mu\nu}$  results the gravitational field equation as

$$G_{\mu\nu} = f(\phi)T_{\mu\nu} + T_{\mu\nu}^{(\phi)}, \quad (2)$$

where the stress-energy density of scalar field expresses

$$T_{\mu\nu}^{(\phi)} = \left( \nabla_\mu \phi \nabla_\nu \phi - \frac{1}{2} g_{\mu\nu} (\nabla \phi)^2 \right) - g_{\mu\nu} V(\phi), \quad (3)$$

and

$$T_{\mu\nu} = \frac{-2}{\sqrt{-g}} \frac{\delta(\sqrt{-g}L)}{\delta g^{\mu\nu}}, \quad (4)$$

is the definition of stress-energy tensor of matter. By considering 00 and  $ii$  components of  $T_{\mu\nu}^{(\phi)}$ , the energy density and pressure could be achieved. After some algebra the conservation equation reads

$$\nabla_\mu (G^{\mu\nu}) = \nabla_\mu [f(\phi)T^{\mu\nu} + T_{(\phi)}^{\mu\nu}] = 0. \quad (5)$$

In addition, the variation of the action 1, w.r.t scalar field gives the evolution equation as

$$\ddot{\phi} + 3H\dot{\phi} = -V(\phi) + \frac{\partial f(\phi)}{\partial \phi} L. \quad (6)$$

Now, by substituting equation 6 into relation 5, two conservation equations for scalar field and matter are attained as

$$\nabla_\mu [T_{(\phi)}^{\mu 0}] = \dot{f}(\phi)L, \quad (7)$$

$$\nabla_\mu [f(\phi)T^{\mu 0}] = -\dot{f}(\phi)L, \quad (8)$$

where over *dot* denotes derivation w.r.t ordinary cosmic time,  $t$ . As it was mentioned in the introduction, the Lagrangian of matter is considered as  $L = L_{(m)} + L_{(de)}$ , [52,54]; where subscript  $m$  denotes matter (cold dark matter and baryons) and  $de$  refers to dark energy. Then the conservation equations could be rewritten as

$$\nabla_\mu [f(\phi)T_{(m)}^{\mu 0}] = -\dot{f}(\phi)L_{(m)}, \quad (9)$$

$$\nabla_\mu [f(\phi)T_{(de)}^{\mu 0}] = -\dot{f}(\phi)L_{(de)}, \quad (10)$$

$$\nabla_\mu [T_{(\phi)}^{\mu 0}] = \dot{f}(\phi)(L_{(m)} + L_{(de)}). \quad (11)$$

By combining the relation 2 and above equations, it is easy to receive

$$\nabla_\mu [T_{(\phi)}^{\mu 0} + f(\phi)T_{(de)}^{\mu 0}] = \dot{f}(\phi)L_{(m)}. \quad (12)$$

In the next step, by virtue of the definition of  $T_{\mu\nu}^{(\phi)}$  and equation 2, the Einstein tensor is modified as

$$G^{\mu\nu} = f(\phi) \left[ T_{(m)}^{\mu\nu} + T_{(de)}^{\mu\nu} + \frac{1}{f(\phi)} T_{(\phi)}^{\mu\nu} \right]. \quad (13)$$

Hereafter, we postulate that both scalar field and dark energy, behave the same as perfect fluid, thence for such perfect mixture the effective stress-energy tensor is obtained as follows

$$T_{(DE)}^{\mu\nu} = T_{(de)}^{\mu\nu} + \frac{1}{f(\varphi)} T_{(\varphi)}^{\mu\nu}, \quad (14)$$

where subscript  $DE$  denotes effective dark energy. Therefore using equations 7-14, the modified Einstein equation and conservation relations are attained as

$$G^{\mu\nu} = f(\varphi) \left[ T_{(m)}^{\mu\nu} + T_{(DE)}^{\mu\nu} \right], \quad (15)$$

$$\nabla_\mu \left[ f(\varphi) T_{(m)}^{\mu 0} \right] = -\dot{f}(\varphi) L_{(m)}, \quad (16)$$

$$\nabla_\mu \left[ f(\varphi) T_{(DE)}^{\mu 0} \right] = \dot{f}(\varphi) L_{(m)}. \quad (17)$$

It should be noticed that, in the right hand side of above equations, only  $L_{(m)}$  is appeared. In fact it could be concluded that the energy, for different components of the Universe is not conserved separately. In refs.[55,56,57], it has been shown that, for perfect fluids, that do not couple directly to the other components of the Universe, there are different Lagrangian densities are equivalent. Namely, one can find that the two Lagrangian densities  $L_{(m)} = P$  and  $L_{(m)} = -\rho$  give the same stress-energy tensor and the equation of motions for all components of the system are similar as well. But in an interacting case, which matter has an interaction with scalar field, the Lagrangian degeneracy is broken. Based on ref.[43], the best choice for such models is  $L_{(m)} = P$ . Using this definition for Lagrangian of the matter one can obtain

$$H^2 = \frac{1}{3} f(\varphi) \left[ \rho_m + \rho_{DE} \right], \quad (18)$$

and also

$$\frac{d}{dt} \left[ f(\varphi) \rho_m \right] + 3H f(\varphi) \rho_m = 0, \quad (19)$$

$$\frac{d}{dt} \left[ f(\varphi) \rho_{DE} \right] + 3H f(\varphi) \left[ 1 + \omega_{DE} \right] \rho_{DE} = 0, \quad (20)$$

where  $H = \dot{a}(t)/a(t)$  is the Hubble parameter,  $a(t)$  is scale factor and  $\omega_{DE}$ , is the EoS parameter of the effective dark energy and satisfies EoS equation as

$$P_{DE} = \omega_{DE} \times \rho_{DE}. \quad (21)$$

To establish an accurate link between theoretical results and observations, one can use the red shift parameter,  $z$ , instead of the scale factor; these two cosmological parameters have a relation as

$$\frac{a(t_0)}{a(t)} = 1 + z \quad \dot{z} = -(1 + z)H. \quad (22)$$

Thus substituting equation 22 into 19 and 20, one finds out

$$f(\varphi) \rho_m = f_0 \times \rho_{m0} \times (1 + z)^3, \quad (23)$$

$$f(\varphi) \rho_{DE} = f_0 \times \rho_{DE0} \times \exp \left[ \int_0^z 3 \frac{1 + \omega_{DE}(\tilde{z})}{1 + \tilde{z}} d\tilde{z} \right], \quad (24)$$

where  $\rho_{DE0}$  and  $\rho_{m0}$  refer to energy densities of dark energy and matter at present time, respectively.

## 2.1 Hubble parameter

Dimensionless Hubble parameter and density parameters could be defined as

$$E(z) = \frac{H(z)}{H_0}, \quad (25)$$

$$\bar{\Omega}_{m0} = \frac{\rho_{m0}}{3H_0^2}, \quad (26)$$

$$\bar{\Omega}_{DE0} = \frac{\rho_{DE0}}{3H_0^2}. \quad (27)$$

The dimensionless density parameters could be rewritten as

$$\Omega_{m0} = \frac{f_0 \times \rho_{m0}}{3H_0^2}, \quad (28)$$

$$\Omega_{DE0} = \frac{f_0 \times \rho_{DE0}}{3H_0^2}. \quad (29)$$

Therefore using relations 18 and 25, the dimensionless Hubble parameter is obtained as follows

$$E^2(z) = \Omega_{m0}(1 + z)^3 + \Omega_{DE0} \exp \left[ \int_0^z 3 \frac{1 + \omega_{DE}(\tilde{z})}{1 + \tilde{z}} d\tilde{z} \right] \quad (30)$$

## 2.2 Coincidence parameter

The ratio of dark matter and dark energy is defined as coincidence parameter and could be obtained as

$$r = \frac{\rho_m}{\rho_{DE}} \quad (31)$$

$$= r_0(1 + z)^3 \exp \left[ -3 \int_0^z \frac{1 + \omega_{DE}(\tilde{z})}{1 + \tilde{z}} d\tilde{z} \right].$$

Also one can obtain

$$\frac{dr}{dz} = \frac{-3\omega_{DE}(z)}{1 + z} r(z). \quad (32)$$

Due to the role of this parameter,  $r$ , in the investigation of the cosmic evolution, it attracts more attention in observational investigations. In fact one can observe that, this importance is arisen from the relation between the EoS parameter and the evolution of  $r$ .

## 2.3 Deceleration Parameter

To investigate the acceleration of the Universe, one can use deceleration parameter which is defined as

$$q(t) = \frac{-1}{a(t)H^2} \frac{d^2 a(t)}{dt^2}. \quad (33)$$

The above equation can be rewritten as

$$q(z) = -1 + \frac{3}{2} \left( \frac{(1 + \omega_{DE})E^2 - \Omega_{m0}(1 + z)^3 \omega_{DE}}{(1 + z)E^2} \right). \quad (34)$$

In present epoch of the Universe evolution, deceleration parameter is determined as

$$q_0 = \frac{1}{2} + \frac{3}{2} \left[ 1 - \Omega_{m0} \right] \omega_{DE}(0). \quad (35)$$

To solve the above equation we introduce an ansatz for EoS parameter as [54, 58]

$$\omega_{DE}(z) = -1 + \omega_0 + \omega_1(1+z)^\beta, \quad (36)$$

where  $\omega_0$ ,  $\omega_1$  and  $\beta$  are free parameters of the model, where the minimum value of  $\chi^2$  of them will be obtained in fitting part. Also it is notable if we choose  $\beta = 0$ , the model reduces to EoS constant models (for instance  $\Lambda$ CDM) [54]. By substituting 36 in 30, the dimensionless Hubble parameter is attained as follows

$$E^2(\{z; P_i\}) = \Omega_{m0}(1+z)^3 + \Omega_{DE0}(1+z)^{3\omega_0} \times \exp\left[3\frac{\omega_1}{\beta}((1+z)^\beta - 1)\right], \quad (37)$$

where

$$\{z; P_i\} = \{\Omega_{m0}, \omega_0, \omega_1, \beta\}, \quad (38)$$

and  $\{P_i\}$  is a set of free parameters which should be determined using data fitting process. Using equation (36), one can rewrite the equations 23, 24 and 31, respectively as

$$f(\varphi)\rho_m = f_0\rho_{m0} \times (1+z)^3, \quad (39)$$

$$f(\varphi)\rho_{DE} = f_0\rho_{DE0} \times (1+z)^{3\omega_0} \times \exp\left[3\frac{\omega_1}{\beta}((1+z)^\beta - 1)\right], \quad (40)$$

and

$$r(z) = r_0(1+z)^{-3(1-\omega_0)} \exp\left[-3\frac{\omega_1}{\beta}((1+z)^\beta - 1)\right]. \quad (41)$$

### 3 A brief review as to cosmological observational data sets

In this section, we should emphasis that the analysis is restricted to the background level, and do not include perturbations. In the following, we want to compare our theoretical results with observations. To this end, we consider four important data sets including SNeIa, CMB, BAO and OHD. In some papers, it was claimed OHD, which obtained versus red shift, is comparable with SNeIa data set, for instance we refer reader to reference [7] and references which are there. This subject motivated us to investigate the effects of this new data set beside other observations to improve the theoretical results. As it will be discussed, the results of OHD although is not independent of SNeIa and BAO data sets [7] but has not any dependency to CMB. Also there are two ways to study CMB and BAO data point among the full parameter distribution and Gaussian which in follow the latter will be used.

#### 3.1 Supernovae type Ia

It is explicit that, supernovae attract more attention in empirical cosmology. Whereas they are very luminous, people

interested to consider them, also for instance at closer distances (i.e. lower redshift) they could be used to calculate Hubble parameter, and for farther distances (i.e. higher redshift) they attain an important role to estimate deceleration parameter  $q$ . It is obvious there are uncertainties of different nature: statistical or random errors and systematic errors. In this work it is remarkable the systematic errors for SNeIa and OHD are neglected. In reality there is always a limit on statistical accuracy, besides the trivial one that time for repetitions is limited. The assumption of independence is violated in a very specific way by so-called systematic errors which appear in any realistic experiment. For instance experiments in nuclear and particle physics usually extract the information from a statistical data sample. The precision of the results then is mainly determined by the number  $N$  of collected reactions. Besides the corresponding well defined statistical errors, nearly every measurement is subject to further uncertainties, the systematic errors, typically associated with auxiliary parameters related to the measuring apparatus, or with model assumptions. The result is typically presented in the form

$$x = 2.34 \pm 0.06 = 2.34 \pm 0.05(stat) \pm 0.03(syst).$$

The only reason for the separate quotation of the two uncertainties is that the size of the systematic uncertainties is less well known than that of the purely statistical error [60]. By virtue of the likelihood functions, one able to estimate the minimum value of  $\chi^2$  for the set of parameters  $\{p_i\}$ , as

$$\mathcal{L}(\{p_i, \mu_0\}) \propto \exp\left[-\frac{1}{2}\chi_{SNe}^2(\{p_i, \mu_0\})\right], \quad (42)$$

where

$$\chi_{SNe}^2(\{p_i, \mu_0\}) = \sum_{n=1}^{557} \frac{[\mu_{obs}(z_n) - \mu_{th}(z_n; \{p_i, \mu_0\})]^2}{\sigma_n^2}. \quad (43)$$

In 43,  $\mu_{obs}(z_n)$  is the observational distance modulus for  $n$ th supernova,  $\sigma_n$  is the variance of the measurement and  $\mu_{th}(z_n)$  is the theoretical distance modulus for  $n$ th supernova which defined as

$$\mu_{th}(z_n; \{p_i, \mu_0\}) = 5 \log_{10} [D_L(z_n; \{p_i\})] + \mu_0,$$

$$\mu_0 = 42.38 - 5 \log_{10} [h],$$

$$D_L(z_n; \{p_i\}) = (1+z) \int_0^z \frac{dz}{E(\bar{z}; \{p_i\})},$$

where  $D_L$  is the luminous distance and  $h = 100 \text{ km s}^{-1} \text{ Mpc}^{-1}$ . To achieve best fit of free parameters, one can marginalize likelihood function w.r.t  $\mu_0$  [59, 60]. Thence  $\chi_{SNe}^2(\{p_i\})$  reduces to

$$\chi_{SNe}^2(\{p_i\}) = A - \frac{B^2}{C}, \quad (44)$$

where  $A$ ,  $B$  and  $C$  are defined as follows

$$A = \sum_{n=1}^{557} \frac{[\mu_{obs}(z_n) - \mu_{th}(z_n; \{p_i, \mu_0 = 0\})]^2}{\sigma_n^2}, \quad (45)$$

$$B = \sum_{n=1}^{557} \frac{\mu_{obs}(z_n) - \mu_{th}(z_n; \{p_i, \mu_0 = 0\})}{\sigma_n^2}, \quad (46)$$

$$C = \sum_{n=1}^{557} \frac{1}{\sigma_n^2}. \quad (47)$$

### 3.2 Cosmic Microwave Background

According to oscillations appear in matter and radiation fields Doppler peaks in radiation (photon) spectrum are produced. Also it should be noted that existence of dark energy, affects the place of the Doppler peaks in spectrum diagrams. To determine the shift of these peaks, theoretically, CMB shift parameters is defined as refs. [1, 61]

$$R_{th}(z_{rec}; \{p_i\}) = \sqrt{\frac{\Omega_{m0}}{f_0}} \int_0^{z_{rec}} \frac{d\tilde{z}}{E(\tilde{z}; \{p_i\})}. \quad (48)$$

In CMB investigations [62], the  $\chi_{CMB}^2$  function versus CMB shift parameter is

$$\chi_{CMB}^2(\{p_i\}) = \frac{[R_{obs} - R_{th}(z_{rec}; \{p_i\})]^2}{\sigma_R^2} \quad (49)$$

where  $R_{obs} = 1.725$ ,  $\sigma_R = 0.018$  and  $z_{rec} \approx 1091.3$  are observational quantities of CMB shift parameter, uncertainty of  $R$  in  $\sigma_1$  confidence level and recombination redshift, respectively refs. [61, 1].

### 3.3 Baryonic Acoustic Oscillations

As in [63] mentioned, because BAO can be considered as a standard length scale at a wide range of redshift it is an useful candidate for cosmological models testing. The importance of BAO mechanism is related to its ability in estimation the contents and curvature of the Universe. One can establish a relation between theoretical BAO parameter,  $A_{th}$ , and dimensionless Hubble parameter, Eq.(30), as

$$A_{th}(z_b; \{p_i\}) = \sqrt{\frac{\Omega_{m0}}{f_0}} [E(z_b; \{p_i\})]^{-1/3} \left[ \frac{1}{z_b} \int_0^{z_b} \frac{d\tilde{z}}{E(\tilde{z}; \{p_i\})} \right]^{2/3}, \quad (50)$$

where  $z_b = 0.35$  [5, 6]. Also  $\chi_{BAO}^2$  in BAO mechanism investigation is as follows

$$\chi_{BAO}^2(\{p_i\}) = \frac{[A_{obs} - A_{th}(z_{rec}; \{p_i\})]^2}{\sigma_A^2}, \quad (51)$$

and also  $A_{obs} = 0.469(n_s/0.98)^{-0.35}$  and  $n_s = 0.968$ , [6, 59]. It is obvious that, the BAO are detected in the clustering of the combined 2dFGRS and SDSS main galaxy samples, and measure the distance-redshift relation at  $z = 0.2$ . But we consider BAO in the clustering of the SDSS luminous red galaxies in which measure the distance-redshift relation at  $z = 0.35$  [64].

### 3.4 Observational Hubble Data

We suggest that, if people want to investigate the accuracy of any theoretical model, it is better, maybe, to consider SNeIa, CMB, BAO and OHD together. In [7], it was claimed that three different models of dark energy i.e.  $\Lambda$ CDM,  $\phi$ CDM and XCDM have been investigated just by considering  $H(z)$  measurement. But they have used  $\bar{H}_0 = 68 \pm 2.8$  and  $\bar{H}_0 = 73.8 \pm 2.4$  which risen from SNeIa data [8]. Therefore it is realized that for the comparison between theoretical results and observations only OHD could not be considered. The  $\chi_{OHD}^2$  function parameter based on OHD data set is defined as

$$\chi_{OHD}^2(\{p_i, H_0\}) = \sum_{n=1}^{28} \frac{[H_{obs}(z_n) - H_0 E_{th}(z_n; \{p_i\})]^2}{\sigma_n^2}, \quad (52)$$

after marginalize w.r.t  $H_0$ , to calculate likelihood,  $\chi_{OHD}^2$  could be considered as

$$\chi_{OHD}^2(\{p_i\}) = A_H - \frac{B_H^2}{C_H}, \quad (53)$$

where

$$A_H = \sum_{n=1}^{28} \frac{[H_{obs}(z_n)]^2}{\sigma_n^2}, \quad (54)$$

$$B_H = \sum_{n=1}^{28} \frac{H_{obs}(z_n) \times E_{th}(z_n; \{p_i\})}{\sigma_n^2}, \quad (55)$$

$$C_H = \sum_{n=1}^{28} \frac{[E_{th}(z_n; \{p_i\})]^2}{\sigma_n^2}. \quad (56)$$

In above equations subscript *obs* is refer to observational quantities and subscript *th* is for theoretical one.

## 4 Cosmological constraints and data fitting

As it was mentioned, we have introduced an ansatz as equation 36, that consist of three free parameters. Where  $\omega_1$  indicates present time value of  $\omega_{DE}$ . For more convenience we can suppose  $\omega_0 = f_0 = 1$  and therefore Eq.(36) is reduced to [54, 58]

$$\omega_{DE}(z) = \omega_1 (1 + z)^\beta. \quad (57)$$

Also, the mean square of relative error functions  $\chi^2$ , normally cause the free parameters plane split in two parts. People usually are interested to the regions which  $\chi^2/N \leq 1$ , where  $N$  denotes the amount of observational data. Whereas we use *Union-2* data set for SNeIa,  $N$  for supernovae is  $N_{SNe} = 557$ , and also for OHD, CMB and BAO, one has  $N_{OHD} = 28$ ,  $N_{CMB} = 1$  and  $N_{BAO} = 1$ . Since in this work three free parameters are appeared, the space of constraints has three dimensions. Thence for better expression, one can map figures on two dimensions (in fact it is supposed that, the free parameters are independent) and their values will be



analyzed. The common regions for best fitting of all constraints, play key role in this study. Based on above discussions we plot a couple of free parameters in Figures 4 - 6. In Figure 4 we investigate the constraints on  $\Omega_{m0}$  in  $\omega_1\beta$  plane, and also for two constraints SNeIa and OHD minimum points of  $\chi^2$  are distinguished. In Figures 5 using best value of  $\omega_1$ , the constraints in  $\Omega_{m0}\beta$  are obtained, in a similar way for best value of  $\beta$ , the behavior of constraints in  $\omega_1\Omega_{m0}$  surface will be shown. Let us, return our attention to figure 4 again. For  $\Omega_{m0} = 0.2$ , the CMB, BAO and OHD have an overlap region, but they are not in agreement with SNeIa results. Also for a different quantity, the SNeIa and OHD results could be in agreement with together. This different behavior of constraints indicates that if one wants to compare theoretical results with observations, it is better the greatest set of constraints, to be considered. For more investigation about overlaps and the effects of individual observations, we plot figures 7 and 8. In figure 7 the behaviour of  $\chi_T^2 = \chi_{\text{SNe}}^2 + \chi_{\text{OHD}}^2 + \chi_{\text{CMB}}^2 + \chi_{\text{BAO}}^2$  and  $\chi_T^2 = \chi_{\text{SNe}}^2 + \chi_{\text{CMB}}^2 + \chi_{\text{BAO}}^2$  for  $\Delta\chi_T^2 = 3.53, 6.25, 8.02$  are compared. Also in figure 8 to investigate degeneracy one can consider  $\chi_T^2 = \chi_{\text{SNe}}^2 + \chi_{\text{OHD}}^2 + \chi_{\text{CMB}}^2 + \chi_{\text{BAO}}^2$  and  $\chi_T^2 = \chi_{\text{OHD}}^2 + \chi_{\text{CMB}}^2 + \chi_{\text{BAO}}^2$  for  $\Delta\chi_T^2 = 0.1, 0.2, 0.3$ . These two figures indicate that although the importance of individual OHD data surveying (in comparison SNeIa, CMB and BAO) is not so important, but it decreases the degeneracy between free parameters of the model. From figures 7 and 8, it is obvious that a collective of four constraints has completely different results in comparison to even three constraints. In the following, by means of observations, we use some custom quantities which are considered for better estimation of theoretical parameters of the model. Since all free parameters of the model are independent, the total likelihood function could be introduced as

$$\mathcal{L}_T = \mathcal{L}_{\text{SNe}} \times \mathcal{L}_{\text{OHD}} \times \mathcal{L}_{\text{CMB}} \times \mathcal{L}_{\text{BAO}}, \quad (58)$$

therefore the total  $\chi^2$  function could be achieved as

$$\chi_T^2 = \chi_{\text{SNe}}^2 + \chi_{\text{OHD}}^2 + \chi_{\text{CMB}}^2 + \chi_{\text{BAO}}^2. \quad (59)$$

It is considerable to attain the maximum amount of the probability and the minimum value of  $\chi^2$ , we should minimize  $\chi_T^2$ . Also it should be noted, in 59 all components have same weight. So the likelihood method is equivalent to this fact that, for instance all measurements which lead to CMB is equal to a supernova explosion!. Afterwards we return to this problem. Another quantity which could be used for data fitting process is

$$\tilde{\chi}^2 = \frac{\chi_T^2}{N_{\text{dof}}} \quad (60)$$

where subscript *dof* is abbreviation of degree of freedom, and  $N_{\text{dof}}$  could be defined as the difference between all observational sources and the amount of free parameters. Let's

explain it in more detail, whereas the amounts of all observations are  $557 + 28 + 1 + 1 = 587$ , and the number of free parameters are 4, by considering  $H_0$ , therefore  $N_{\text{dof}}$ , is equal to 583. Also one knows, the acceptable quantity for  $\tilde{\chi}^2$  is 1.05. For more convenient, we now define the average relative error functions as follows

$$\bar{\chi}_{\text{SNe}}^2 = \frac{\chi_{\text{SNe}}^2}{N_{\text{SNe}}}, \quad (61)$$

$$\bar{\chi}_{\text{OHD}}^2 = \frac{\chi_{\text{OHD}}^2}{N_{\text{OHD}}}, \quad (62)$$

$$\bar{\chi}_{\text{CMB}}^2 = \frac{\chi_{\text{CMB}}^2}{N_{\text{CMB}}}, \quad (63)$$

$$\bar{\chi}_{\text{BAO}}^2 = \frac{\chi_{\text{BAO}}^2}{N_{\text{BAO}}}. \quad (64)$$

Finally we can introduce  $\chi_m^2$  function, which is equal to maximum of  $\bar{\chi}^2$  functions and it could be considered as

$$\chi_m^2 = \max(\bar{\chi}_{\text{SNe}}^2, \bar{\chi}_{\text{OHD}}^2, \bar{\chi}_{\text{CMB}}^2, \bar{\chi}_{\text{BAO}}^2). \quad (65)$$

In fact the  $\chi_m^2$  function could be considered as a criterion of accuracy for the models. Now we want to compare the behavior of  $\chi_m^2$  and  $\tilde{\chi}^2$  functions. Without loss the generality of the model, one can plot the three dimensional shape of  $\chi_m^2$  and  $\tilde{\chi}^2$ , versus free parameters of the model. These diagrams help us to find out the best estimation of the free parameters in comparison to observations; for more clarity one can see the figure 9. In this figure, the first diagram shows the minimum of  $\chi_m^2$  and  $\tilde{\chi}^2$  versus  $\Omega_{m0}$ . Also in two latest diagrams of figure 9, the minimum points are drawn based on  $\omega_1$  and  $\beta$  respectively. By comparison the behavior of these relative error functions in Figure 9 one can realize that, there are more points (or neighborhood) in which  $\tilde{\chi}^2 < 1$ , but  $\chi_m^2$  exceeds 1.05. In fact this behavior was predictable, because in definition of  $\tilde{\chi}^2$ , we use the contribution of all observational data set. So, for example the  $\chi_{\text{CMB}}^2$  deviation of best fitting results, could be recompense by SNeIa data abundance. We will return to this drawback, after some discussion about likelihood and relative error functions. For more illustration, we portrait the different surfaces of three dimensional,  $(\Omega_{m0}, \omega_1, \beta)$ , to  $(\Omega_{m0}, \beta)$ ,  $(\omega_1, \Omega_{m0})$  and  $(\omega_1, \beta)$  surfaces, which are brought in Figures 10, 11 and 12. Diagrams B and C are related to  $(\chi_T^2)_{\text{min}}$ , where the subscript *min*, shows the minimum value of  $\chi_T^2$ . It is notable, in a three dimensional space of free parameters, the confidence levels 68.3%, 90% and 95.4% are proportional to  $\Delta\chi_T^2 = 3.53$ ,  $\Delta\chi_T^2 = 6.25$  and  $\Delta\chi_T^2 = 8.02$  surfaces respectively where  $\Delta\chi_T^2 = \chi_T^2 - (\chi_T^2)_{\text{min}}$ . In diagram B of Figures 10, 11 and 12 the counter lines of confidence levels are drawn and in diagram C, both the  $\chi_m^2$  surfaces and counter lines are brought for more comparison. From diagram C it is realized that the confidence level counters exceed the  $\chi_m^2$  regions. From this behaviour it is concluded that, the theoretical prediction of CMB shift parameter is very greater than it's observational quantity. As mentioned heretofore, when the total mean square error function is introduced the weight of all constraints was identical and this

causes some problems. As a matter of fact, the results of likelihood's parameter, equation 59, the effect of CMB shift parameter in comparison to the abundant SNeIa data set is ignored. For more information, one can see Table 2 and definition of  $N_{dof}$ . To overcome these problems, we redefine  $\chi^2_T$  as bellow

$$\chi^2_T = \chi^2_{SNe} + \chi^2_{OHD} + 3\chi^2_{CMB} + 3\chi^2_{BAO}. \quad (66)$$

It should be noted, in data fitting and maximization of probability quantities these two definitions of  $\chi^2_T$ , i.e. equations 59 and 66, have not very different. For justifying this claim one can compare Tables 2 and 3 which are related to 59 and 66 respectively. But in figures which related to confidence levels one can observe that the exceeding of confidence levels are reduced, therefore the re-weight of some constraints can improve the behaviour of the model. For more clarification one can refer to figures 13, 14 and 15. Now by means of 66, we margin the likelihood  $\mathcal{L}(\Omega_{m0}, \omega_1, \beta)$  w.r.t  $\omega_1$ ,  $\beta$  and  $\Omega_{m0}$  respectively. Also the relative probability functions  $\mathcal{L}(\Omega_{m0}, \beta)$ ,  $\mathcal{L}(\omega_1, \Omega_{m0})$  and  $\mathcal{L}(\omega_1, \beta)$  in two dimensional confidence levels 68.3%, 90% and 95.4% are plotted in Figure 16. For more investigations, we will draw the one dimensional marginalized likelihood functions  $\mathcal{L}(\Omega_{m0})$  versus  $\Omega_{m0}$ ,  $\mathcal{L}(\omega_1)$  based on  $\omega_1$  and  $\mathcal{L}(\beta)$  versus  $\beta$  in figure 17. Meanwhile in Table 4 one observes the quantities which maximize the marginalized likelihoods using different confidence levels by means of confidence levels  $\sigma_1 = 68.3\%$  and  $\sigma_2 = 95.4\%$ .

#### 4.1 Typical example

Now, we define an effective dark energy as combination of dark energy  $\rho_{de}$  and scalar field density as  $\rho_{DE} = \rho_{de} + \rho_\phi/f(\phi)$ . So, the Friedmann equation is rewritten as

$$3H^2 = f(\phi)(\rho_m + \rho_{DE}). \quad (67)$$

An useful parameter in this study is energy density parameter  $\Omega$ . Here  $\Omega_{DE}$  and  $\Omega_m$  respectively will be taken equal to  $\Omega_{DE} = f(\phi)\rho_{DE}/\rho_c$  and  $\Omega_m = f(\phi)\rho_m/\rho_c$ , in which  $\rho_c$  is the critical energy density which is defined as  $\rho_c = 3H^2$ . As a result, from the Friedmann equation we have  $\Omega_{DE} + \Omega_m = 1$ .

To obtain energy conservation equations for effective dark energy one can achieve the following results

$$\frac{d}{dt}(f(\phi)\rho_{DE}) + 3Hf(\phi)(1 + \omega_{DE})\rho_{DE} = \gamma\rho_m\dot{f}(\phi), \quad (68)$$

$$\frac{d}{dt}(f(\phi)\rho_m) + 3Hf(\phi)(1 + \gamma)\rho_m = -\gamma\rho_m\dot{f}(\phi), \quad (69)$$

so that the effective pressure of dark energy is defined as  $p_{DE} = p_\Lambda + p_\phi/f(\phi)$ , and one has the effective dark energy equation of state parameter as  $\omega_{DE} = p_{DE}/\rho_{DE}$ . Also  $\gamma$  is

the matter equation of state parameter which is defined as  $\gamma = p_m/\rho_m$ . For  $\gamma = \text{constant}$ , integrating of Eq.(69) results in the following relation for cold dark matter energy density

$$\rho_m = \frac{\rho_{em}^0}{a^{3(1+\gamma)}f^{(1+\gamma)}(\phi)}, \quad (70)$$

where  $\rho_{em}^0 = f_0^{(1+\gamma)}(\phi)\rho_m^0$ . In this step, we suppose that the effective dark energy could be defined as ADE, in other word we assume that

$$\rho_{DE} \equiv \rho_{ADE} = \frac{3n^2}{T^2}, \quad (71)$$

where  $n$  is a numerical constant and  $T$  is cosmic time and therefore  $\Omega_{DE}$  is obtained as  $\Omega_{DE} = f(\phi)n^2/H^2T^2$ . Taking this assumption and using Eq.(68), the equation of state parameter of effective dark energy could be acquired as

$$\omega_{DE} = -1 + \frac{2}{3} \frac{1}{n} \sqrt{\frac{\Omega_{DE}}{f(\phi)}} + \frac{\dot{f}(\phi)}{3Hf(\phi)}(\gamma r - 1), \quad (72)$$

where  $r$  is ratio of cold dark matter and effective dark energy, namely  $r = \rho_m/\rho_{DE} = \Omega_m/\Omega_{DE}$ . The interaction term in this model generates an extra term for  $\omega_{DE}$ , which can justify the phantom divide line crossing. By definition an ansatz for  $\omega_{e\Lambda}$ , it can be considered as

$$\omega_{e\Lambda} + 1 = \omega_0 + \omega_1(1+z)^\beta. \quad (73)$$

For fitting the free parameters for ADE in an external scalar field interaction model, we use the 557 Union-2 sample database of *SNeIa*, and  $\rho_m = \rho_{\text{radiation}} + \rho_{\text{baryon}} + \rho_{\text{darkmatter}}$ . Therefore in this case the Friedmann equation is as

$$3H^2 = f(\phi)(\rho_m + \rho_{DE}). \quad (74)$$

Combining Eqs.(68)-(71), give

$$3H^2 = f(\phi)\left(\frac{\rho_{em}^0}{a^{3(1+\gamma)}f^{(1+\gamma)}(\phi)} + \frac{3n^2}{T^2}\right), \quad (75)$$

where  $\rho_{em}^0$  is the effective energy density of matter at the present time. Whereas the 557 Union-2 sample database have collected from red shift parameter to various *SNeIa*, therefore we rewrite  $E = H/H_0$  versus  $z$  as

$$E^2 = \frac{r_0(1+z)^3 + (1+z)^{3\omega_0} \exp\left\{3\frac{\omega_1}{\beta}[(1+z)^\beta - 1]\right\}}{r_0 + 1}. \quad (76)$$

To achieve the best fit for free parameters based on subsection 3.1 a minimization method leads to

$$\chi^2_{sn_{min}}(\omega_0 = 1.1; \omega_1 = -1.65; \beta = -2.25), \quad (77)$$

$$\chi^2_{min} = A - \frac{B^2}{C} = 542.75, \quad (78)$$

$$\mu_0 = -\frac{B}{C} = 43.1089. \quad (79)$$

where implies  $\chi^2_{sn}/dof = \chi^2_{sn_{min}}/dof = 0.981(dof = 553)$ . In figure 1, we show a comparison between theoretical distance modulus and observed distance modulus of supernovae

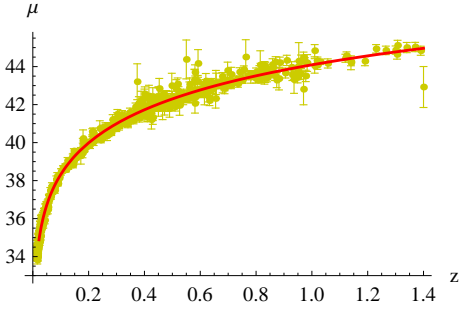


**Fig. 1** The observed distance modulus of supernovae (points) and the theoretical predicted distance modulus (red-solid line) in the context of ADE model.

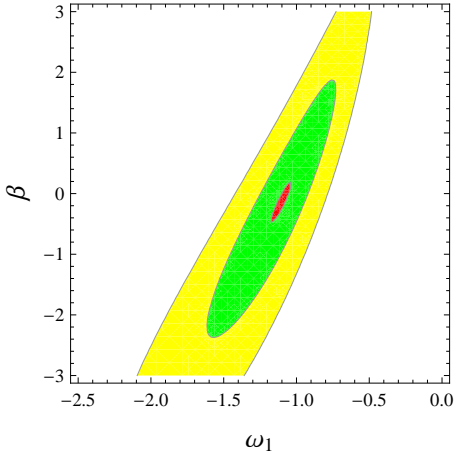


**Fig. 2** Contour plots for the free parameters  $\omega_1$  and  $\beta$ , shows that the best value for these parameters are  $-1.86 < \omega_1 < -1.62$  and  $-2.27 < \beta < -0.73$ .

data. The red-solid line indicates the theoretical value of distance modulus,  $\mu_{th}$ , for the best value of free parameters  $\omega_1 = -1.65$ ,  $\omega_0 = 1.1$  and  $\beta = -2.25$ . This shows that the model is clearly consistent with the data since  $\chi^2/dof = 1$ . Fig.2 show contour plots for the free parameters  $\omega_1$  and  $\beta$ , it is shown that the best value for these parameters are  $-1.86 < \omega_1 < -1.62$  and  $-2.27 < \beta < -0.73$  in which for stability condition  $c^2 > 0$ , we have taken the interface between green and yellow sector,  $\omega_1 = -1.68$ .

The evolution of effective dark energy parameter,  $\omega_{DE}$ , versus  $z$ , for  $\omega_0 = 1.1$ ,  $\omega_1 = -1.68$  and  $\beta = -2.25$  have been shown in Fig.3. This show that by growing  $z$  the parameter get into the phantom phase.

Here  $\omega_0$ ,  $\omega_1$  and  $\beta$  are free parameters of the model which obtained from data fitting. It is clear that, if the form of dark energy density is given the coupling function,  $f(\varphi)$ , could be easily determined. For instance by using Eqs.(68), (69) and (71) one can obtain

$$f(\varphi) = f_0 t^2 a^{-3\omega_0} \exp \left[ 3\omega_1 \frac{(z+1)^{\beta+2}}{\beta+2} \right], \quad (80)$$

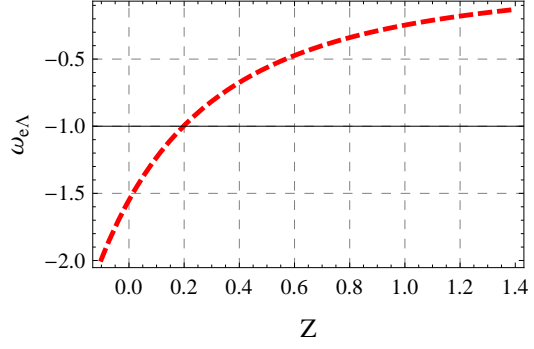


**Fig. 3** The plot shows the evolution of effective dark energy parameter,  $\omega_{DE}$ , versus  $z$ , for  $\omega_0 = 1.1$ ,  $\omega_1 = -1.68$  and  $\beta = -2.25$ .

here  $f_0$  is the constant of integration. Whereas

$$\frac{\dot{f}(\varphi)}{f(\varphi)} = 3H \left[ \frac{2}{3tH} - \omega_0 - \omega_1 (1+z)^{\beta+2} \right].$$

A significant result of observational data is accelerated expansion of the Universe. A good cosmological model should be able to describe this acceleration. An useful quantity to investigate this property of the Universe is deceleration parameter which defined as  $q = -1 - \dot{H}/H^2$ . Using Eqs.(67), (68) and (69), one achieves the deceleration parameter gives

$$q = -1 + \frac{3}{2} \left[ 1 - \omega_0 - \omega_1 (1+z)^{\beta} \right] \times \left( \frac{D_0}{1 + (1+z)^{3(1-\omega_0)}(t) \exp \left[ \frac{-3\omega_1(1+z)^{\beta}}{\beta} \right]} \right), \quad (81)$$

where  $D_0$  is the constant of integration. It is clearly seen that for  $\omega_0 = 1.1$ ,  $\omega_1 = -1.68$ ,  $\beta = -2.25$ , (which have obtained from data fitting processes)  $q < 0$ .

## 5 Conclusion and Discussion

Interacting models which contain an external interaction between matter and scalar fields attract more attentions. Such mechanisms are capable to suppress the fifth force and also are in good agreement with observations. Using such powerful mechanism we have attained some cosmological parameters consist of coincidence and deceleration parameters. For instance based on Table 2, and equations 32 and 34 it is clear that  $r(z)$  is a decreasing function and  $q$  has taken negative values for different amounts of  $z$ . Considering a suitable ansatz for EoS parameter of effective dark energy dimensionless Hubble parameter is obtained. So by means of SNeIa, CMB, BAO and OHD data sets the minimum value of  $\chi^2$  for the free parameters of the model are achieved. To estimate the free parameters of an ansatz for the effective dark energy equation of state, the whole of the observational data sets have been considered. For more details one can compare the results of figures 7 and 8, and the results of typical example, subsection 4.1. Also for getting better overlap between the counters with the constraint  $\chi_m^2 \leq 1$ ,



the  $\chi^2_T$  function have been re-weighted. Meanwhile the relative probability functions have plotted for marginalized likelihood  $\mathcal{L}(\Omega_{m0}, \omega_1, \beta)$  according to two dimensional confidence levels 68.3%, 90% and 95.4%. In addition the value of free parameters which maximize the marginalized likelihoods using above confidence levels have obtained. Based on above discussions a couple of free parameters in figures 4 - 6, have plotted. In figure 4, the constraints on  $\Omega_{m0}$  in  $\omega_1 \beta$  plane have investigated; and also, for two constraints SNeIa and OHD minimum points of  $\chi^2$  have distinguished. In figures 5, using best value of  $\omega_1$ , the constraints in  $\Omega_{m0} \beta$  surface are obtained. In a similar way, for best value of  $\beta$ , the behavior of constraints in  $\omega_1 \Omega_{m0}$  plane have shown. Also based on figure 4, for  $\Omega_{m0} = 0.2$ , the CMB, BAO and OHD have an overlap region, but they are not in agreement with SNeIa results; where one possible explanation would be an incompatibility among the data sets. Also, for a different values one can find a region which SNeIa and OHD are in more agreement against CMB and BAO. This different behavior of constraints indicates that, if one wants to compare theoretical and observational results, it maybe better the greatest set of constraints to be considered. For more investigation about overlaps and the effects on individual observations, the figures 7 and 8, have been plotted. In figure 7, the behaviour of  $\chi^2_T = \chi^2_{SNe} + \chi^2_{OHD} + \chi^2_{CMB} + \chi^2_{BAO}$  and  $\chi^2_T = \chi^2_{SNe} + \chi^2_{CMB} + \chi^2_{BAO}$  for  $\Delta\chi^2_T = 3.53, 6.25, 8.02$ , have compared. Also in figure 8, we have considered  $\chi^2_T = \chi^2_{SNe} + \chi^2_{OHD} + \chi^2_{CMB} + \chi^2_{BAO}$  and  $\chi^2_T = \chi^2_{OHD} + \chi^2_{CMB} + \chi^2_{BAO}$ , for  $\Delta\chi^2_T = 0.1, 0.2, 0.3$ , to investigate the degeneracy. These two figures indicate that although the importance of individual OHD data surveying in cosmological investigations (in comparison SNeIa, CMB and BAO) is not so important but it decreases degeneracy between free parameters.

**Acknowledgements** H. Sheikahmadi would like to thank Iran's National Elites Foundation for financially support during this work.

## References

1. G. Efstathiou and J. R. Bond, *Cosmic Confusion: Degeneracies among Cosmological Parameters Derived from Measurements of Microwave Background Anisotropies*, *Mon. Not. Roy. Astron. Soc.* **304** (1999) 75.
2. J. Dunkley, et al., *Five-Year Wilkinson Microwave Anisotropy Probe (WMAP) Observations: Bayesian Estimation of CMB Polarization Maps*, *Astrophys. J.* **701** (2009) 1804.
3. A. G. Riess et al., *Observational Evidence from Supernovae for an Accelerating Universe and a Cosmological Constant*, *Astron. J.* **116** (1998) 1009.
4. S. Perlmutter, et al., *Measurements of  $\Omega$  and  $\Lambda$  from 42 High-Redshift Supernovae*, *Astrophys. J.* **517** (1999) 565.
5. D. J. Eisenstein and W. Hu, *Baryonic Features in the Matter Transfer Function*, *Astrophys. J.* **496** (1998) 605.
6. M. Shoji, D. Jeong and E. Komatsu, *Extracting Angular Diameter Distance and Expansion Rate of the Universe from Two-dimensional Galaxy Power Spectrum at High Redshifts: Baryon Acoustic Oscillation Fitting versus Full Modeling*, *Astrophys. J.* **693** (2009) 1404.
7. O. Farooq and B. Ratra, , *Hubble parameter measurement constraints on the cosmological deceleration-acceleration transition redshift*, *arXiv: 1301.5243* (2013).
8. G. Chen, J. R. Gott and B. Ratra, *Non-Gaussian Error Distribution of Hubble Constant Measurements*, *Publ. Astron. Soc. Pac.* **115**(2003) 1269.
9. M. Tegmark, et al., *Cosmological parameters from SDSS and WMAP*, *Phys. Rev. D* **69** (2004) 103501.
10. J. Sollerman, et al., *First-Year Sloan Digital Sky Survey-II (SDSS-II) Supernova Results: Constraints on Non-Standard Cosmological Models*, *Astrophysical Journal* **703** (2009) 1374.
11. D. N. Spergel, et al., *First-Year Wilkinson Microwave Anisotropy Probe (WMAP) Observations: Determination of Cosmological Parameters*, *Astrophys. J. suppl* **148** (2003) 175.
12. G. Hinshaw, et al., *Five-Year Wilkinson Microwave Anisotropy Probe (WMAP) Observations: Data Processing, Sky Maps, and Basic Results*, *Astrophys. J. Suppl* **180** (2009) 225.
13. S. Weinberg, *The cosmological constant problem*, *Rev. Mod. Phys.* **61** (1989) 1.
14. S. M. Carrol, *The Cosmological Constant*, *Living Rev. Relativity* **4** (2001) 1.
15. C. Brans and R. H. Dicke, *Mach's Principle and a Relativistic Theory of Gravitation*, *Phys. Rev* **124** (1961) 925.
16. Y. Fujii, *Origin of the gravitational constant and particle masses in scale invariant scalar-tensor theory*, *Phys. Rev. D* **26** (1982) 2580.
17. S. M. Carroll, *Quintessence and the rest of the world*, *Phys. Rev. Lett.* **81** (1998) 3067.
18. E. N. Saridakis, S. V. Sushkov, *Quintessence and phantom cosmology with non-minimal derivative coupling*, *Phys. Rev. D.* **81** (2010) 083510.
19. M. R. Garousi, *Tachyon couplings on non-BPS D-branes and Dirac-Born-Infeld action*, *Nucl. Phys. B* **584** (2000) 284.
20. D. Kutasov and V. Niarchos, *Tachyon effective actions in open string theory*, *Nucl.Phys. B* **666** (2003) 56.
21. J. M. Cline, S. Jeon, and G. D. Moore, *The phantom menaced: Constraints on low-energy effective ghosts*, *Phys. Rev. D* **70** (2004) 043543.
22. P. Singh, M. Sami, and N. Dadhich, *Cosmological dynamics of phantom field*, *Phys. Rev. D* **68** (2003) 023522.
23. X. Chen, Y. Gong, E. N. Saridakis, *Phase-space analysis of interacting phantom cosmology*, *JCAP* **0904**, 2009 001.
24. H. Wei, R. G. Cai and D. F. Zeng, *Hessence: A New View of Quintom Dark Energy*, *Class.Quant.Grav* **22** (2005) 3189.
25. D. Kutasov and V. Niarchos, *Cosmological Evolution of a Quintom Model of Dark Energy*, *Phys. Lett. B* **608** (2005) 177.
26. M. Malquarti, E. J. Copeland, and A. R. Liddle, *k-essence and the coincidence problem*, *Phys. Rev. D.* **68** (2003) 023512.
27. C. Bonvin, C. Caprini, and R. Durrer, *A no-go theorem for k-essence dark energy*, *Phys. Rev. Lett* **97** (2006) 081303.
28. N. Birrell and P. Davies, *Quantum fields in curved space*. (Cambridge University Press, 1982);
29. V. Mukhanov and S. Winitzki, *Introduction to quantum effects in gravity*. (Cambridge University Press, Cambridge, 2007).
30. H. Sheikahmadi, A. Aghamohammadi and Kh. Saaidi *Vacuum quantum fluctuations in quasi de Sitter background* *arXiv: gr-qc/1407.0125*.
31. L. Susskind, *Strings, Black Holes and Lorentz Contraction*, *arXiv: hep-th/9308139* ;
32. L. Susskind, *The World as a Hologram*, *Arxiv: hep-th/9409089*.
33. D. Kutasov and V. Niarchos, *Some Speculations About Black Hole Entropy In String Theory*, *Arxiv: hep-th/9309145*.
34. B. Guberina, R. Horvat, and H. Nikolic, *Nonsaturated Holographic Dark Energy*, *Axiv: astro-ph/0611299*.
35. A. Aghamohammadi, K. Saaidi, and M. R. Setare, *Holographic dark energy with time depend gravitational constant in the non-flat Hořava-Lifshitz cosmology*, *Astrophys. Space. Sci.* **332**, 2011 503.

36. A. Aghamohammadi, K. Saaidi, *Holographic dark energy and  $f(R)$  gravity*, *Physica Scripta* **83**, 2011 025902.
37. R. G. Cai, *A Dark Energy Model Characterized by the Age of the Universe*, *Phys. Lett. B.* **657** (2007) 228.
38. H. Wei and R. G. Cai, *A New Model of Agegraphic Dark Energy*, *Phys. Lett. B.* **660** (2008) 113.
39. H. Wei and R. G. Cai, *Cosmological Constraints on New Agegraphic Dark Energy*, *Phys. Lett. B.* **663** (2008) 1.
40. J. Khoury and A. Weltman, *Chameleon cosmology*, *Phys. Rev. D* **69** (2004) 044026.
41. J. Khoury and A. Weltman, *Chameleon Fields: Awaiting Surprises for Tests of Gravity in Space*, *Phys. Rev. Lett.* **93** (2004) 171104.
42. D. F. Mota and J. D. Barrow, *Tachyon effective actions in open string theory*, *Phys. Lett. B* **581** (2004) 141.
43. Kh. Saaidi, *(Non-)geodesic motion in chameleon Brans Dicke model*, *Astrophys. Space. Sci.* **345** (2013) 431.
44. S.W. Hawking and G. F. R. Ellis, *The Large Scale Structure of Spacetime*, (Cambridge University Press, Cambridge (1973)).
45. G. W. Gibbons and S.W. Hawking, *Action integrals and partition functions in quantum gravity*, *Phys. Rev. D.* **15** (1997) 2752.
46. J. D. Brown, and J. W. York, *Microcanonical functional integral for the gravitational field*, *Phys. Rev. D.* **47** (1993) 1420.
47. Kh. Saaidi, A. Mohammadi, H. Sheikahmadi,  *$\gamma$  parameter and Solar System constraint in chameleon Brans Dicke theory*, *Phys. Rev. D.* **83**, 2011 104019.
48. Kh. Saaidi, H. Sheikahmadi, T. Golanbari, and S.W. Rabiei, *On the holographic dark energy in chameleon scalar-tensor cosmology*, *Astrophys. Space. Sci.* **348**, 2013 233.
49. N. Banerjee, S. Das and K. Ganguly *Chameleon field and the late time acceleration of the universe*, *Pramana* **74** L481 2010.
50. S. Das and N. Banerjee, *Brans-Dicke Scalar Field as a Chameleon*, *Phys. Rev. D.* **78** 043512 (2008).
51. H. Farajollahi, A. Salehi, *Attractors, Statefinders and Observational Measurement for Chameleonic Brans–Dicke Cosmology*, *JCAP* **1011** 2010 006.
52. H. Farajollahi, A. Salehi, F. Tayebi, *Entropy and statefinder diagnosis in chameleon cosmology*, *Astrophys. Space. Sci.* **335**, 2011 629.
53. Kh. Saaid, H. Sheikahmadi and J. Afzali, *Chameleon mechanism with a new potential*, *Astrophys. Space. Sci.* **333** 2011 501.
54. A. Aghamohammadi, Kh. Saaidi, A. Mohammadi, H. Sheikahmadi, T. Golanbari, and S.W. Rabiei, *Effect of an external interaction mechanism in solving agegraphic dark energy problems*, *Astrophys. Space. Sci.* **345**, 2013, 17.
55. S. Carroll, *Quintessence and the Rest of the World: Suppressing Long-Range Interactions* *Phys. Rev. Lett.* **81**, ( 1998) 3067.
56. T. Damour and A. M. Polyakov, *The String Dilaton and a Least Coupling Principle*, *Nucl. Phys. B* **423**, ( 1994) 532.
57. C. F. Will, *Theory and Experiment in Gravitational Physics* (Cambridge: CUP, 1981).
58. S. del Campo, J. C. Fabris, R. Herrera, W. Zimdahl *On holographic dark-energy models*, *Phys.Rev.D* **83**, 2011 123006.
59. R. Amanullah, et al., *Spectra and Light Curves of Six Type Ia Supernovae at  $0.511 < z < 1.12$  and the Union2 Compilation*, *Astrophys. J* **716** (2010) 712.
60. G. Bohm and G. Zech, *Introduction to Statistics and Data Analysis for Physicists* (Verlag Deutsches Elektronen-Synchrotron, 2010).
61. Y. Wang and P. Mukherjee, *Robust Dark Energy Constraints from Supernovae, Galaxy Clustering, and Three-Year Wilkinson Microwave Anisotropy Probe Observations*, *Astrophys. J.* **650** (2006) 1.
62. E. Komatsu et al., *Seven-Year Wilkinson Microwave Anisotropy Probe (WMAP) Observations: Cosmological Interpretation*, *Astrophys. J. Suppl. Ser.* **192** (2011) 18.
63. N. G. Busca, et al., *Baryon Acoustic Oscillations in the Ly – forest of BOSS quasars*, *arXiv: 1211.2616* (2012).
64. F. C. Solano, U. Nucamendi *Reconstruction of the interaction term between dark matter and dark energy using SNeIa, BAO, CMB,  $H(z)$  and X-ray gas mass fraction*, *arXiv:1207.0250* [astro-ph.CO].
65. C. Zhang et al., *Four New Observational  $H(z)$  Data From Luminous Red Galaxies of Sloan Digital Sky Survey Data Release Seven*, *arXiv: 1207.4541* [astro-ph.CO] (2012).
66. J. Simon, , L. Verde and R. Jimenez, *Constraints on the redshift dependence of the dark energy potential*, *Phys. Rev. D* **71** (2005) 123001.
67. M. Moresco, et al., *New constraints on cosmological parameters and neutrino properties using the expansion rate of the Universe to  $z$  1.75*, *J. Cosmology Astropart. Phys.* **07** (2012) 053.
68. C. H. Chuang and Y. Wang, *Modeling the Anisotropic Two-Point Galaxy Correlation Function on Small Scales and Improved Measurements of  $H(z)$ ,  $D_A(z)$ , and  $f(z)$  from the Sloan Digital Sky Survey DR7 Luminous Red Galaxies*, *arXiv: 1209.0210* [astro.ph-CO] (2012).
69. C. Blake et al., *The WiggleZ Dark Energy Survey: joint measurements of the expansion and growth history at  $z < 1$* , *MNRAS*, **425** (2012) 405.
70. D. Stern et al., *Cosmic chronometers: constraining the equation of state of dark energy. I:  $H(z)$  measurements* *J. Cosmology Astropart. Phys.*, **02** (2010) 008.

**Table 1** In this table from left to right  $z$ ,  $H(z)(\text{km s}^{-1} \text{Mpc}^{-1})$ , it's uncertainty  $\sigma_H(\text{km s}^{-1} \text{Mpc}^{-1})$  in measurement and related references (by considering the technique which is used) are collected, respectively.

| $z$   | $H(z)$ | $\sigma_H$ | References | Technique                |
|-------|--------|------------|------------|--------------------------|
| 0.070 | 69     | 19.6       | [65]       | SDSS DR7; $0 < z < 0.4$  |
| 0.100 | 69     | 12         | [66]       | ATC; $0.1 < z < 1.8$     |
| 0.120 | 68.6   | 26.2       | [65]       | SDSS DR7; $0 < z < 0.4$  |
| 0.170 | 83     | 8          | [66]       | ATC; $0.1 < z < 1.8$     |
| 0.179 | 75     | 4          | [67]       | OHD+CMB; $0 < z < 1.75$  |
| 0.199 | 75     | 5          | [67]       | OHD+CMB; $0 < z < 1.75$  |
| 0.200 | 72.9   | 29.6       | [65]       | SDSS DR7; $0 < z < 0.4$  |
| 0.270 | 77     | 14         | [66]       | ATC; $0.1 < z < 1.8$     |
| 0.280 | 88.8   | 36.6       | [65]       | SDSS DR7; $0 < z < 0.4$  |
| 0.350 | 76.3   | 5.6        | [68]       | SDSS DR7 LRGs; $z=0.35$  |
| 0.352 | 83     | 14         | [67]       | OHD+CMB; $0 < z < 1.75$  |
| 0.400 | 95     | 17         | [66]       | ATC; $0.1 < z < 1.8$     |
| 0.440 | 82.6   | 7.8        | [69]       | WiggleZ+H(z); $z < 1.0$  |
| 0.480 | 97     | 62         | [70]       | CMB+OHD; $0.2 < z < 1.0$ |
| 0.593 | 104    | 13         | [67]       | OHD+CMB; $0 < z < 1.75$  |
| 0.600 | 87.9   | 6.1        | [69]       | WiggleZ+H(z); $z < 1.0$  |
| 0.680 | 92     | 8          | [67]       | OHD+CMB; $0 < z < 1.75$  |
| 0.730 | 97.3   | 7.0        | [69]       | WiggleZ+H(z); $z < 1.0$  |
| 0.781 | 105    | 12         | [67]       | OHD+CMB; $0 < z < 1.75$  |
| 0.875 | 125    | 17         | [67]       | OHD+CMB; $0 < z < 1.75$  |
| 0.880 | 90     | 40         | [70]       | CMB+OHD; $0.2 < z < 1.0$ |
| 0.900 | 117    | 23         | [66]       | ATC; $0.1 < z < 1.8$     |
| 1.037 | 154    | 20         | [67]       | OHD+CMB; $0 < z < 1.75$  |
| 1.300 | 168    | 17         | [66]       | ATC; $0.1 < z < 1.8$     |
| 1.430 | 177    | 18         | [66]       | ATC; $0.1 < z < 1.8$     |
| 1.530 | 140    | 14         | [66]       | ATC; $0.1 < z < 1.8$     |
| 1.750 | 202    | 40         | [66]       | ATC; $0.1 < z < 1.8$     |
| 2.300 | 224    | 8          | [63]       | BAO; $0.7 < z < 2.3$     |

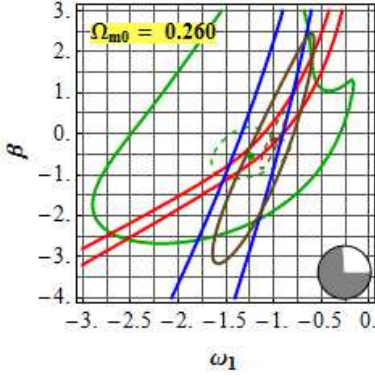


**Fig. 4** The counter lines of  $\chi^2_{SNe} = 557$  (brown),  $\chi^2_{OHD} = 28.0$  (green),  $\chi^2_{CMB} = 1.0$  (red), and  $\chi^2_{BAO} = 1.0$  (blue) for of  $\Omega_{m0} = 0.26$  are plotted. Also for two constraints SNeIa and OHD minimum points of  $\chi^2$  are distinguished. The dashed lines refer to the counter lines which are greater of the minimum points only unity.

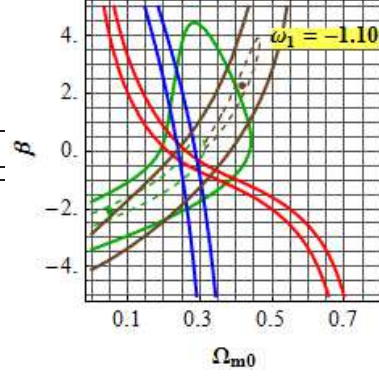


**Fig. 5** The counter lines of  $\chi^2_{SNe} = 557$  (brown),  $\chi^2_{OHD} = 28.0$  (green),  $\chi^2_{CMB} = 1.0$  (red), and  $\chi^2_{BAO} = 1.0$  (blue) for  $\omega_1 = -1.1$  are plotted. Also for two constraints SNeIa and OHD minimum point of  $\chi^2$  are distinguished. The dashed lines refer to the counter lines which are greater of the minimum points only unity.

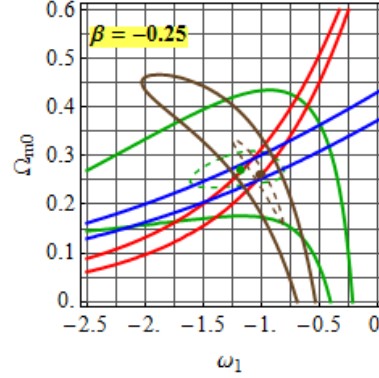


**Fig. 6** The counter lines of  $\chi^2_{SNe} = 557$  (brown),  $\chi^2_{OHD} = 28.0$  (green),  $\chi^2_{CMB} = 1.0$  (red), and  $\chi^2_{BAO} = 1.0$  (blue) for  $\beta = -0.25$  are plotted. Also for two constraints SNeIa and OHD minimum point of  $\chi^2$  are distinguished. The dashed lines refer to the counter lines which are greater of the minimum points only unity.

**Table 2** In the table, the quantities related to minimum point of  $\chi^2_T = \chi^2_{SNe} + \chi^2_{OHD} + \chi^2_{CMB} + \chi^2_{BAO}$  are introduced.

| $\beta$             | $\omega_1$     | $\Omega_{m0}$  | $\chi^2_{BAO}$      |
|---------------------|----------------|----------------|---------------------|
| -0.243              | -1.053         | 0.272          | $16 \times 10^{-4}$ |
| $\chi^2_{CMB}$      | $\chi^2_{OHD}$ | $\chi^2_{SNe}$ | $(\chi^2_T)_{min}$  |
| $12 \times 10^{-5}$ | 16.23          | 542.75         | 558.98              |

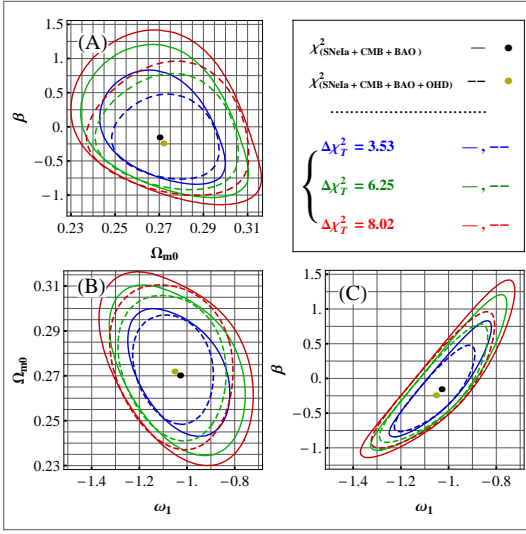


**Fig. 7** In this figure the behaviour of  $\chi_T^2 = \chi_{\text{SNe}}^2 + \chi_{\text{OHD}}^2 + \chi_{\text{CMB}}^2 + \chi_{\text{BAO}}^2$  (dashed counters) and  $\chi_T^2 = \chi_{\text{SNe}}^2 + \chi_{\text{CMB}}^2 + \chi_{\text{BAO}}^2$  (solid counters) for  $\Delta\chi_T^2 = 3.53$  (inner loops),  $6.25$  (middle loops),  $8.02$  (outer loop) are compared. The minimum points of these two  $\chi_T^2$  functions are distinguished by Solid points.

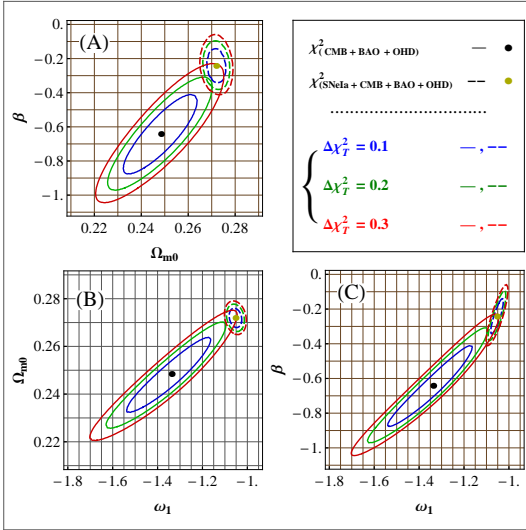


**Fig. 8** In this plot we consider  $\chi_T^2 = \chi_{\text{SNe}}^2 + \chi_{\text{OHD}}^2 + \chi_{\text{CMB}}^2 + \chi_{\text{BAO}}^2$  (dashed counters) and  $\chi_T^2 = \chi_{\text{OHD}}^2 + \chi_{\text{CMB}}^2 + \chi_{\text{BAO}}^2$  (solid counters) for  $\Delta\chi_T^2 = 0.1$  (inner loops),  $0.2$  (middle loops),  $0.3$  (outer loop) to investigate degeneracy in this work. This Figure and Figure 7 indicate that although the importance of individual OHD data surveying in cosmological investigations (in comparison SNe Ia, CMB and BAO) is not so important but it causes decreasing degeneracy between free parameters of the model. The minimum points of these two  $\chi_T^2$  functions are distinguished by Solid points.

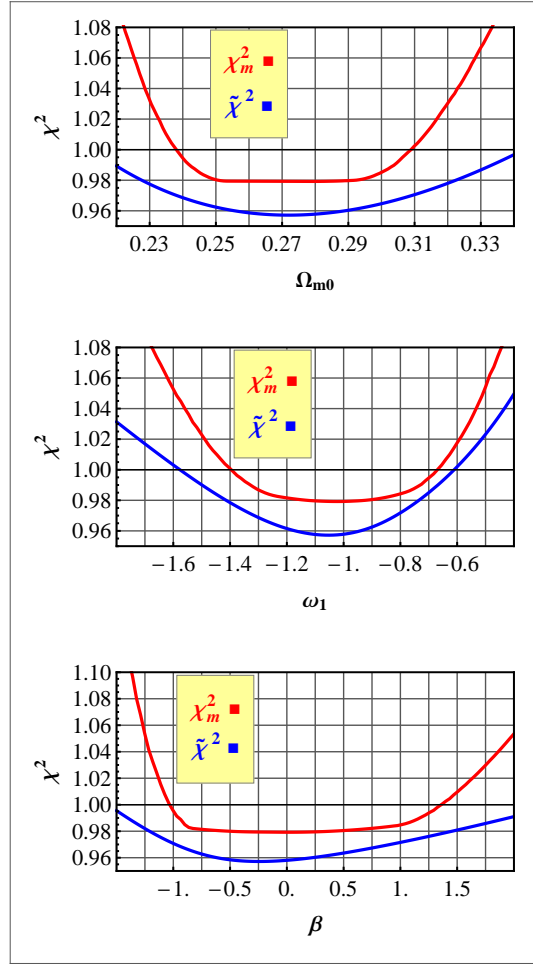


**Fig. 9** In above diagrams the minimum quantity of  $\tilde{\chi}^2$  (blue line) and  $\chi_m^2$  (red-upper-line) versus  $\Omega_{m0}$ ,  $\omega_1$  and  $\beta$  parameters have been drawn respectively.

**Table 3** This table is related to minimum point of  $\chi_T^2 = \chi_{\text{SNe}}^2 + \chi_{\text{OHD}}^2 + 3\chi_{\text{CMB}}^2 + 3\chi_{\text{BAO}}^2$ .

| $\beta$               | $\omega_1$            | $\Omega_{m0}$         | $\chi_{\text{BAO}}^2$ |
|-----------------------|-----------------------|-----------------------|-----------------------|
| -0.239                | -1.051                | 0.272                 | $5 \times 10^{-4}$    |
| $\chi_{\text{CMB}}^2$ | $\chi_{\text{OHD}}^2$ | $\chi_{\text{SNe}}^2$ | $(\chi_T^2)_{\min}$   |
| $8 \times 10^{-10}$   | 16.23                 | 542.75                | 558.98                |



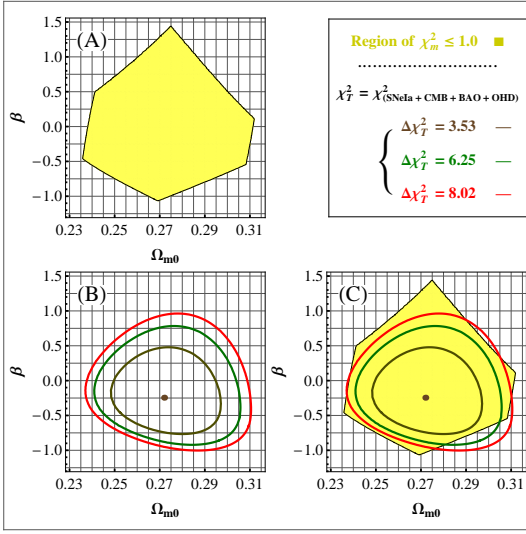


**Fig. 10** In diagram (A), the image of  $\chi_m^2 \leq 1$  on the  $(\Omega_{m0}, \beta)$  surface are portrait. In (B) the minimum point of  $\chi_T^2 = \chi_{\text{SNe}}^2 + \chi_{\text{OHD}}^2 + \chi_{\text{CMB}}^2 + \chi_{\text{BAO}}^2$  and the shadow of  $\Delta\chi_T^2 = 3.53$ (inner loop),  $6.25$ (middle loop),  $8.02$ (outer loop) surfaces on the  $(\Omega_{m0}, \beta)$  plate, are plotted. In part (C) both diagrams (A) and (B) are brought to compare the results.

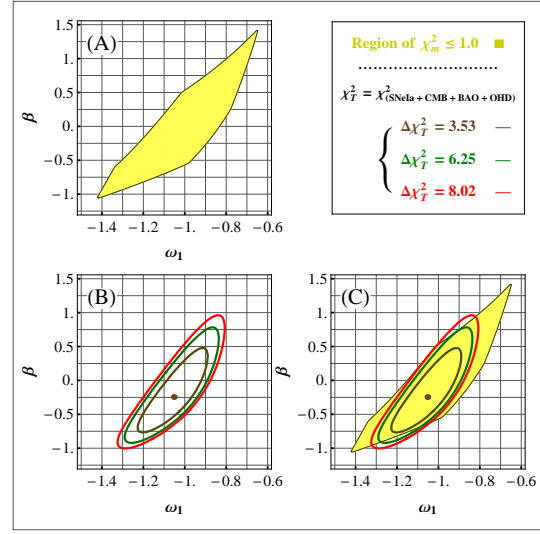


**Fig. 12** In diagram (A), the image of  $\chi_m^2 \leq 1$  on the  $(\omega_1, \beta)$  surface are portrait. In (B) the minimum point of  $\chi_T^2 = \chi_{\text{SNe}}^2 + \chi_{\text{OHD}}^2 + \chi_{\text{CMB}}^2 + \chi_{\text{BAO}}^2$  and the shadow of  $\Delta\chi_T^2 = 3.53$ (inner loop),  $6.25$ (middle loop),  $8.02$ (outer loop) surfaces on the  $(\omega_1, \beta)$  plate, as counter lines, are drawn. In part (C) both diagrams (A) and (B) are compared.

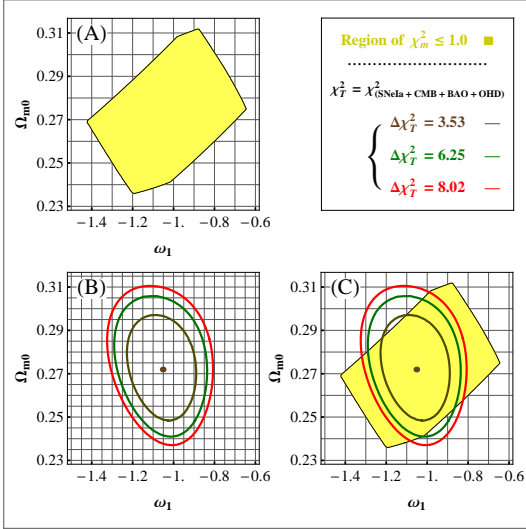


**Fig. 11** In diagram (A), the image of  $\chi_m^2 \leq 1$  on the  $(\omega_1, \Omega_{m0})$  surface are portrait. In (B) the minimum point of  $\chi_T^2 = \chi_{\text{SNe}}^2 + \chi_{\text{OHD}}^2 + \chi_{\text{CMB}}^2 + \chi_{\text{BAO}}^2$  and the shadow of  $\Delta\chi_T^2 = 3.53$ (inner loop),  $6.25$ (middle loop),  $8.02$ (outer loop) surfaces on the  $(\omega_1, \Omega_{m0})$  plate, are drawn. In part (C) both diagrams (A) and (B) are considered for more comparison.

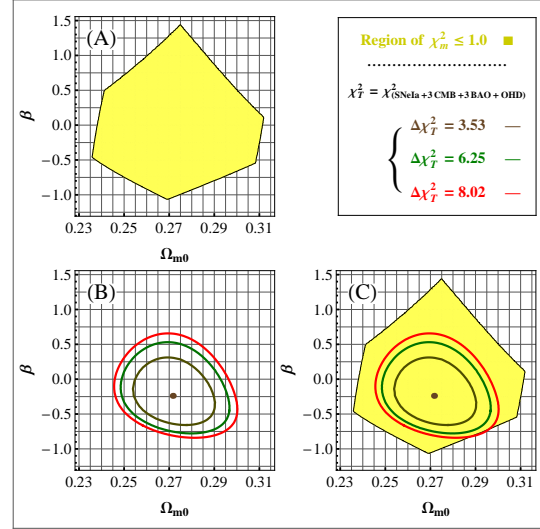


**Fig. 13** In diagram (A), the image of  $\chi_m^2 \leq 1$  on the  $(\Omega_{m0}, \beta)$  surface are portrait. In (B) the minimum point of  $\chi_T^2 = \chi_{\text{SNe}}^2 + \chi_{\text{OHD}}^2 + 3\chi_{\text{CMB}}^2 + 3\chi_{\text{BAO}}^2$  and the shadow of  $\Delta\chi_T^2 = 3.53$ (inner loop),  $6.25$ (middle loop),  $8.02$ (outer loop) surfaces on the  $(\Omega_{m0}, \beta)$  surface, as counter lines, are drawn. In part (C) both diagrams (A) and (B) have been brought for more comparison.

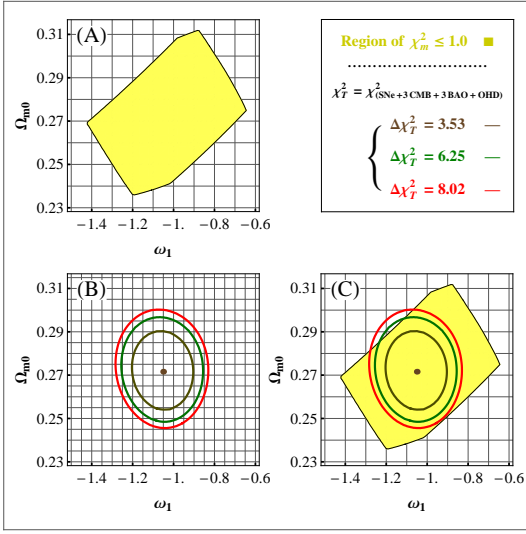


**Fig. 14** In diagram (A), the image of  $\chi_m^2 \leq 1$  on the  $(\omega_1, \Omega_{m0})$  surface are portrait. In (B) the minimum point of  $\chi_T^2 = \chi_{\text{SNe}}^2 + \chi_{\text{OHD}}^2 + 3\chi_{\text{CMB}}^2 + 3\chi_{\text{BAO}}^2$  and the shadow of  $\Delta\chi_T^2 = 3.53$ (inner loop),  $6.25$ (middle loop),  $8.02$ (outer loop) surfaces on the  $(\omega_1, \Omega_{m0})$  plate, as counter lines, are drawn. In part (C) both diagrams (A) and (B) are brought for comparison.

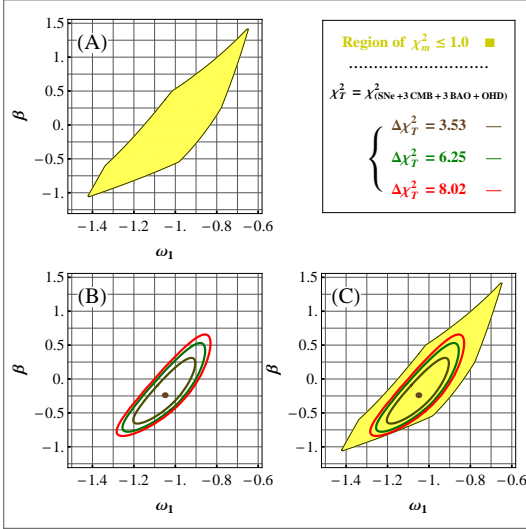


**Fig. 15** In diagram (A), the image of  $\chi_m^2 \leq 1$  on the  $(\omega_1, \beta)$  surface are portrait. In (B) the minimum point of  $\chi_T^2 = \chi_{\text{SNe}}^2 + \chi_{\text{OHD}}^2 + 3\chi_{\text{CMB}}^2 + 3\chi_{\text{BAO}}^2$  and the shadow of  $\Delta\chi_T^2 = 3.53$ (inner loop),  $6.25$ (middle loop),  $8.02$ (outer loop) surfaces on the  $(\omega_1, \beta)$  plate, as counter lines, are drawn. In part (C) both diagrams (A) and (B) are collected for comparison.

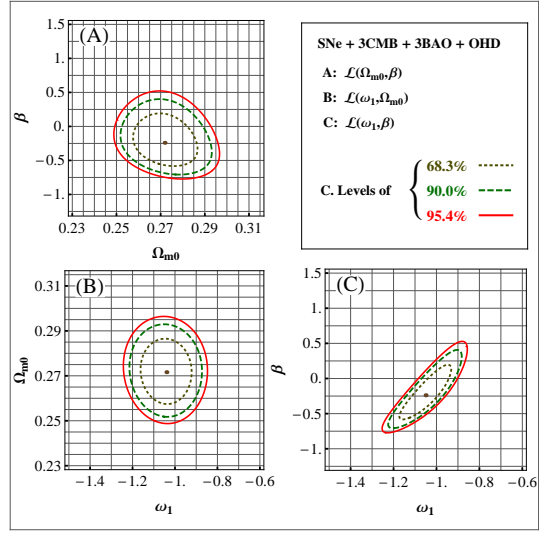


**Fig. 16** In the above two dimensional likelihood diagrams, the 68.3% confidence level (dotted line), 90.0% confidence level (green-dashed-line) and 95.45% confidence level (red-solid-line) after marginalization on the  $\omega_1$ ,  $\beta$  and  $\Omega_{m0}$  free parameters are plotted. Note that in this figure we use  $\chi_T^2 = \chi_{\text{SNe}}^2 + \chi_{\text{OHD}}^2 + 3\chi_{\text{CMB}}^2 + 3\chi_{\text{BAO}}^2$  and also the shadow of  $\Delta\chi_T^2 = 3.53$ (inner loop),  $6.25$ (middle loop),  $8.02$ (outer loop) surfaces.

**Table 4** In this table the quantities which maximize the relative probability functions  $\mathcal{L}(\Omega_{m0})$ ,  $\mathcal{L}(\omega_1)$  and  $\mathcal{L}(\beta)$  using confidence levels  $\sigma_1 = 68.3\%$  and  $\sigma_2 = 95.4\%$  are calculated. The data sets are includes of *SNeIa*, *CMB*, *BAO* and *OHD* in which the weight of  $\chi_{\text{CMB}}^2$  and  $\chi_{\text{BAO}}^2$  in  $\chi_{\text{Total}}^2$  function is the coefficient 3.

| $\sigma_2^-$ | $\sigma_2^+$ | $\sigma_1^-$ | $\sigma_1^+$ | $(\mathcal{L})_{\text{max}}$ | x             |
|--------------|--------------|--------------|--------------|------------------------------|---------------|
| 0.02         | 0.02         | 0.01         | 0.01         | 0.272                        | $\Omega_{m0}$ |
| 0.16         | 0.156        | 0.08         | 0.08         | -1.04                        | $\omega_1$    |
| 0.44         | 0.59         | 0.23         | 0.27         | -0.24                        | $\beta$       |

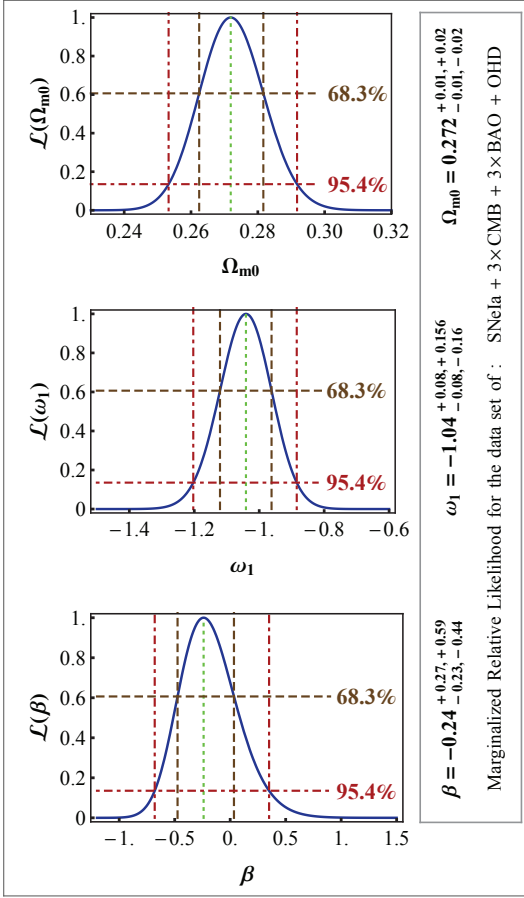


**Fig. 17** In above diagrams the relative likelihoods are plotted. The 68.3% and 95.4% confidence levels are distinguished as brown dashed line and red dot-dash line respectively. It should be noted that in these figure we use  $\chi^2_I = \chi^2_{\text{SNe}} + \chi^2_{\text{OHD}} + 3\chi^2_{\text{CMB}} + 3\chi^2_{\text{BAO}}$ . Also the best fits of the free parameters are as  $\beta = -0.24^{+0.27, +0.59}_{-0.23, -0.44}$ ,  $\omega_1 = -1.04^{+0.08, +0.156}_{-0.08, -0.16}$  and  $\Omega_{m0} = 0.272^{+0.01, +0.02}_{-0.01, -0.02}$ .

